PLASMA PLUME CHARACTERISTICS OF ELECTRIC THRUSTERS

Hirokazu Tahara

Department of Mechanical Science and Bioengineering
Graduate School of Engineering Science, Osaka University
1-3, Machikaneyama, Toyonaka, Osaka 560-8531, Japan
Phone:+81-6-6850-6178
Fax:+81-6-6850-6179
E-mail:tahara@me.es.osaka-u.ac.jp

Abstract

Recently, lots of electric thruster are in practical use because of their high specific impulses suitable for long space missions. The exhaust plasma plume characteristics strongly depend on thruster species. In this study, three kinds of plasma thruster were investigated in order to understand their plasma plume characteristics concerned with thruster performance and spacecraft interaction. Several plasma diagnostic measurements were carried out. The laboratory-model low-power Hall-effect thruster THT-IV, the low-power radiation-cooled arcjet thruster RAT-VII and the quasisteady magnetoplasmadynamic (MPD) arcjet thruster MY-III were operated, and their performances and plasma characteristics are discussed.

1. Introduction

The closed-electron-drift Hall-effect thruster is a promising propulsion device in space. The performance has been improved in Russia since 1960s [1]. Because 1-2 kW class Hall thrusters can achieve a high performance of thrust 50-100 mN and thrust efficiency 40-50 % at specific impulses of 1000-2000 sec, they are expected to be used as main thrusters for near-earth missions in the United States and Europe [2,3]. Even in Japan, the high performance attracts attention of mission planners [4-8]. In Osaka University, an experimental facility was constructed in 1997 to study plasma production and acceleration processes and unstable operational phenomena in low power Hall thrusters and also to examine spacecraft and plasma plume interactions [4,5]. Basic experiments have been made using THT-series low-power Hall thrusters to obtain fundamental operational characteristics. The influences of material, width and length of acceleration channel on thruster performance were mainly investigated [6,7]. As a result, the THT-IIIA thruster could be stably operated in a wide range of magnetic field strength. A high thrust efficiency was achieved with a low discharge current and a high thrust for a preferable magnetic field strength regardless of discharge voltage at a constant mass flow rate. Both the thrust and the specific impulse ranged from 10 to 70 mN and from 1200 to 2300 sec, respectively, at discharge voltages of 200-500 V with mass flow rates of 1-3 mg/s in a wide input power range of 250-1800 W. The thrust efficiency ranged from 30 to 45 %. Furthermore, one-dimensional thruster flowfield calculation, in which an axial motion of ions; axial and azimuthal motions of electrons perpendicular to magnetic field were considered, was carried out [7-9]. The model included first ionization by direct electron-neutral collisions, electron-neutral elastic collisions, electron-ion Coulomb collisions, Bohm diffusion (anomalous diffusion); channel wall losses of ion flux and electron energy flux with secondary electron emission effect. The flowfield in an acceleration channel was divided into diffusion, ionization and ion acceleration regions. Both ionization and acceleration were found to, intensively and efficiently, occur in their thin regions with a few mm thick near the acceleration channel exit. The calculated thruster performance roughly agreed with experimental ones. New Hall thrusters THT-IV and THT-V were designed with all basic research data. With the THT-V thruster with many considerations, long stable operations were achieved [10,11]. In all experiments at 200-400 V with 1.5-3 mg/s, the thrust and the specific impulse ranged from 15 to 70 mN and from 1100 to 2300 sec, respectively, in a low electric power range of 300-1300 W. The thrust efficiency reached 55 %. Hence, a large map of the thruster performance was successfully made. The thermal characteristics were also examined with data of both measured and calculated temperatures in the thruster body. Thermally safe conditions were achieved with all input powers. With both the thermal characteristics and the thruster performance, a flight model is under design.

In the present study, more basic experiments are made using the THT-IV thruster to examine the influences of magnetic field shape and strength, and acceleration channel length on thruster performance and plasma plume characteristics and to establish guidelines for design of high-performance Hall thrusters. Thrust is measured by a pendulum method. Exhaust plasma diagnostic measurement are carried out to evaluate plume divergent angles and voltage utilization efficiencies. Ion current spatial profiles are measured with a Faraday cup, and ion energy distribution functions are estimated from data with a retarding potential analyzer. The characteristics of optimum magnetic field are discussed.

In Osaka University, the electric propulsion research program has focused on the development of a low power radiation-cooled arcjet thruster to replace the monopropellant hydrazine thruster presently used for north-south stationkeeping of geosynchronous satellites [12-15]. This program has been largely successful in demonstrating that the arcjet thruster can be operated with a hydrogen/nitrogen mixture gas at the power levels available on satellites currently in use. The performance characteristics showed that the specific impulse was 350-550 sec, the thrust efficiency 30-45 % and the ratio of thrust to power 100-200 mN/kW in a wide input power range between 300 W and 1 kW. The obtained performance level is expected to offer significant mass or extended satellite life benefit. From viewpoint of practical use in space, it is important to understand exhaust plasma plume characteristics and to estimate interactions between spacecraft and the exhaust plasma. Because the complicated plasma structure is produced inside the arcjet discharge chamber, the inner plasma feature is expected to strongly influence the exhaust plume characteristics [16-20].

In the present study, the laboratory-model radiation-cooled arcjet thruster RAT-VII is operated in a low electric power range of 750-800 W with a mixture of hydrogen and nitrogen simulating hydrazine at mass flow rates of 20-25 mg/s in order to study the exhaust plasma plume characteristics. Electrostatic probe measurements are carried out to evaluate electron temperature, electron number density and Mach number in the downstream plume region [16-21].

The quasisteady magnetoplasmadynamic (MPD) arcjet thruster is a promising thruster for exploration to deep space and for raising orbits of large space structures. The MPD arcjet utilizes principally electromagnetic force, i.e., Lorentz force, which is generated by electromagnetic interaction between discharge current and magnetic field azimuthally induced by the discharge current. The thrust depends only on the discharge current and does not basically on propellant species because of electromagnetic acceleration. However, in an MPD discharge chamber, complicated chemical reactions involving dissociation and ionization are expected to occur together with the acceleration processes [22-25]. Consequently, it has been recognized that the performance characteristics on the discharge voltage, thrust efficiency and electrode erosion depend on propellant species and electrode geometry. However, the exhaust plasma plume feature is still unclear depending on propellant species and electrode geometry.

In the present study, the quasisteady MPD arcjet thruster MY-III is operated to study the exhaust plasma plume characteristics. Both emission spectroscopic and rotatable double probe measurements are made to evaluate electron temperature, plasma number density and plasma flow direction in the downstream plume region.

2. Hall-Effect Thruster

2.1 Experimental Apparatus

The experimental facility, as shown in Fig.1, mainly consists of a water-cooled stainless steel vacuum tank 1.2 m in diameter x 2.25 m long, two compound turbo molecular pumps, several DC power supplies and a thrust measurement system [4-7,10]. The setup is changed in plasma plume diagnostic measurement. The vacuum tank pressure is kept a range of 10^{-3}-10^{-4} Pa under operations. A clean and high vacuum environment can be created by using the oil-free turbo molecular pump system, which is useful to study contamination due to Hall thruster plumes.

Thrusts are measured by a pendulum method, as shown in Fig.1. A Hall thruster is mounted on a thrust stand suspended with an aluminum bar, and the position of the thrust stand is detected by an eddy-current-type gap sensor (non-contacting micro-displacement meter). It has a high sensitivity and a good linearity. Thrust calibration is conducted with a weight and pulley arrangement which is able to apply a known force to the thrust stand under vacuum environment. With this design, friction force was small, and it resulted in no measurable hysteresis.

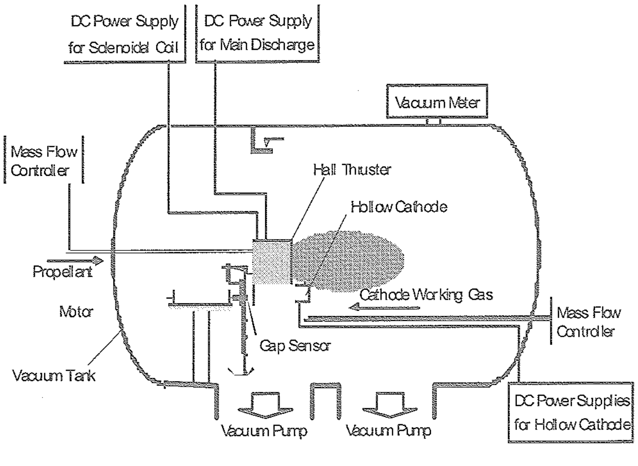

Fig.1 Experimental facility of Hall thruster for thrust measurement.

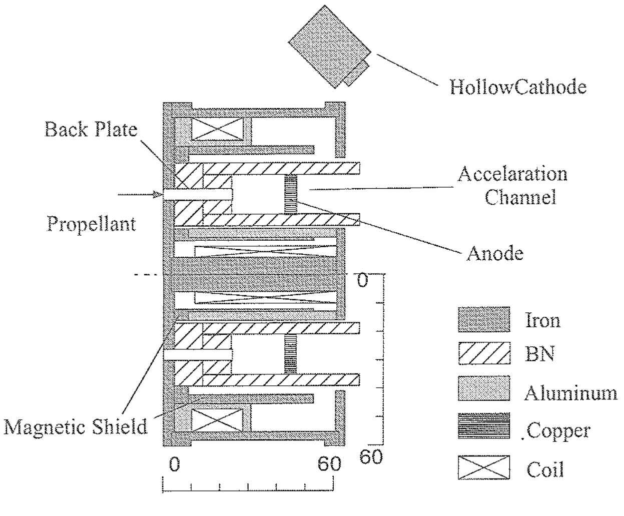

Fig.2 Cross sectional view of THT-IV Hall thruster.

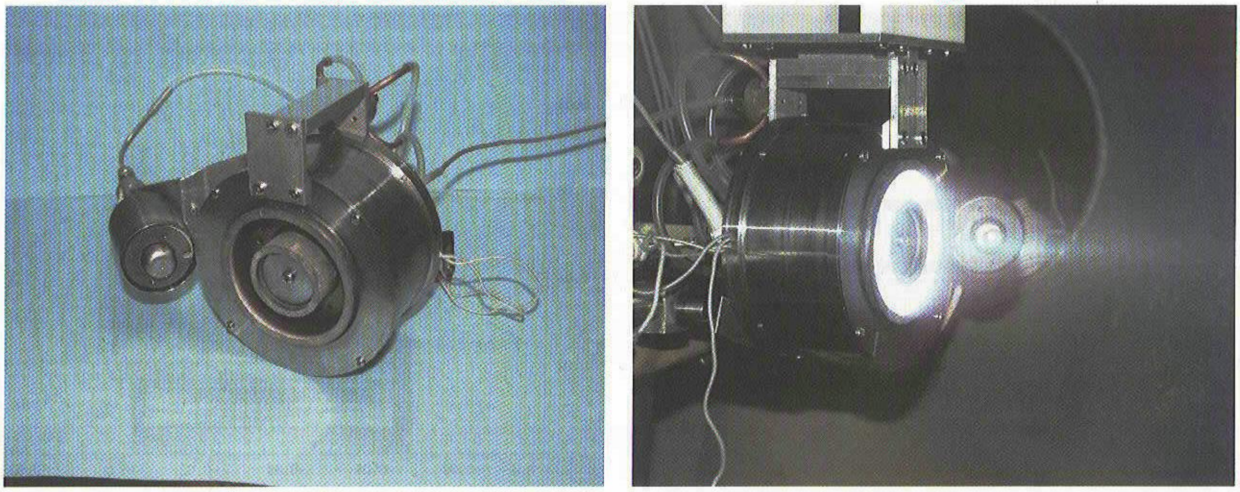

(a) Thruster overview (b) Operation

Fig.3 Photographs of THT-IV thruster overview and operation.

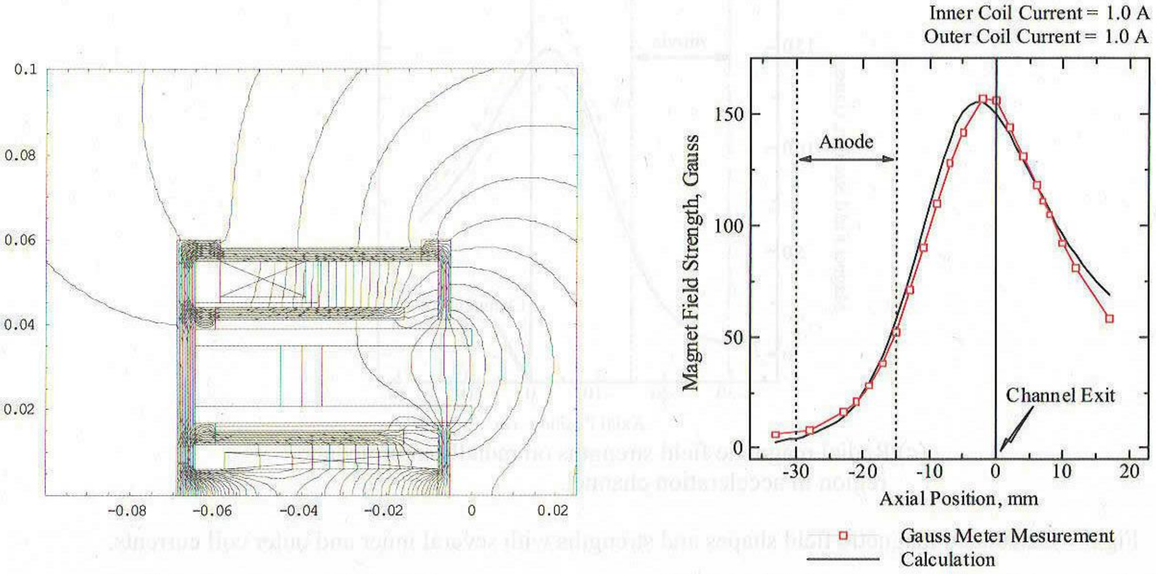

(a) Calculated magnetic field shape. (b) Calculated and measured radial magnetic field strengths on radially intermediate region in acceleration channel.

Fig.4 Magnetic field shape and strength with inner and outer coil currents of 1 and 1 A.

The THT-IV thruster, as shown in Figs.2 and 3, has an acceleration channel with an outer diameter of 70 mm and an inner diameter of 42 mm, i.e., with 14 mm in width, and the channel length can be changed from 15 to 30 mm. The wall material of the acceleration channel is boron nitride (BN) ceramics. The anode is made of copper. The hollow cathode (Iontech HCN-252) is used as the main cathode. After propellant gas is introduced from 4 lines into a plenum chamber behind the anode, it is uniformly injected from 24 ports azimuthally drilled on the anode into the acceleration channel.

The thruster has the magnetic coils on the central axis and on the inner surface of the outer cylinder. Because the two coil currents can be separately controlled, magnetic field shape and strength in the acceleration channel can be changed in order to find out optimum magnetic field structure. Figure 4 shows the magnetic field shape and strength with an inner coil current of 1 A and an outer one of 1 A. In Fig.4(b), the radial magnetic field strengths on the radially intermediate region in the acceleration channel are presented. The measurement was made with a Gauss meter. The calculated magnetic field strength agrees with the measured one. The magnetic field strength decreases as distance to

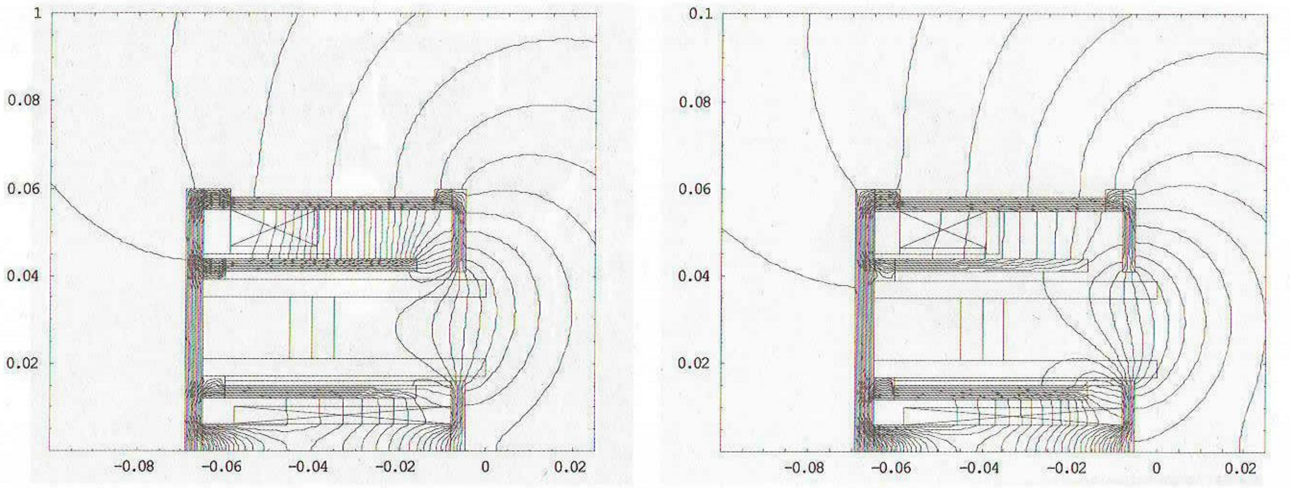

(a) With inner and outer coil currents of 0.75 and 1.5 A. (b) With 1.25 and 0.5 A.

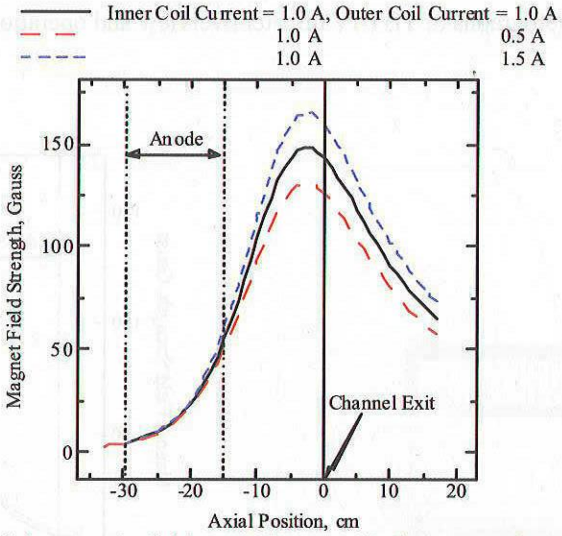

(c) Radial magnetic field strengths on radially intermediate region in acceleration channel.

Fig.5 Calculated magnetic field shapes and strengths with several inner and outer coil currents.

the anode decreases, and it has a maximum near the channel exit and a minimum at the anode. Figure 5 shows the magnetic field shapes and strengths calculated with inner and outer coil currents of 0.75 and 1.5 A; 1.25 and 0.5 A. Although the all axial variations in radial magnetic field strength, as shown in Fig.5(c), have a same maximum of about 150 Gauss near the channel exit, the field shapes are extremely different. When the ratio of inner coil current to outer one increases from 0.75/1.5 to 1.25/0.5, the downstream directions perpendicular to magnetic field lines near the channel exit are changed from radially-inward directions to radially-outward ones. Accordingly, because main discharge location and ion trajectory can be roughly predicted from these characteristics, ionization process in the acceleration channel, ion losses on the channel wall and plasma plume feature are inferred.

Xenon is used as propellants. In a series of experiments, discharge currents and thrusts are measured with varying discharge voltage, mass flow rate, magnetic field shape and strength, and acceleration channel length; specific impulses and thrust efficiencies are evaluated. Exhaust plasma diagnostic measurement is carried out to evaluate plume divergent angles and voltage utilization efficiencies. Ion current spatial profiles are measured with a Faraday cup, and ion energy distribution functions are estimated from data with a retarding potential analyzer (RPA). The Faraday cup and the RPA are located at 20 cm downstream from the thruster exit, and a motor rapidly, semi-circularly moves them.

2.2 Results and Discussion

2.2.1 Thruster performance

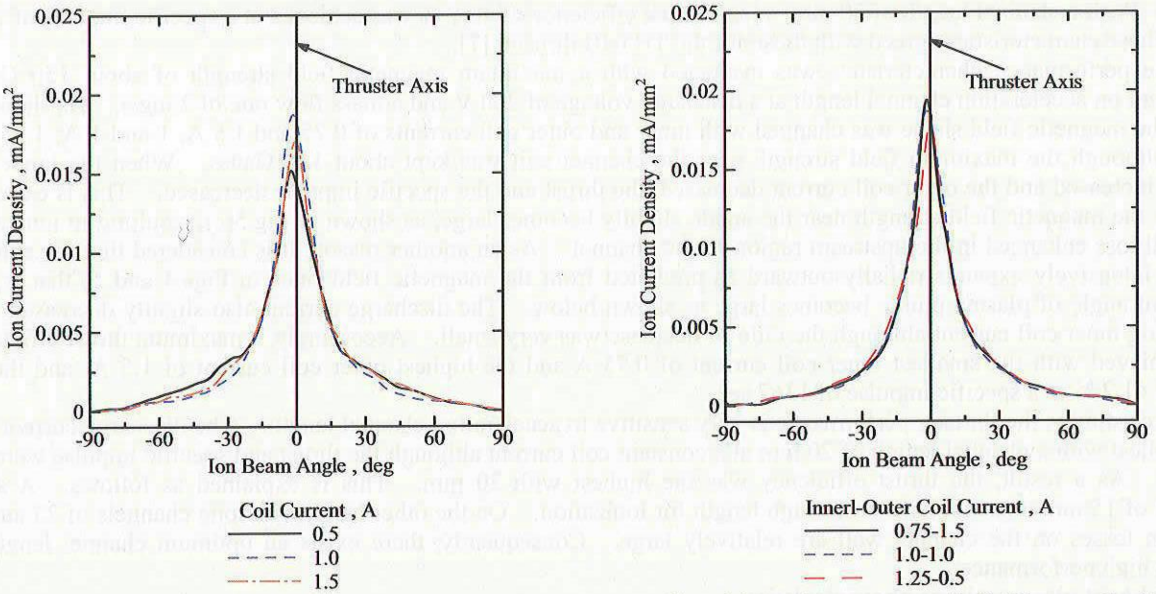

(a) With inner and outer coil current ratio of 1:1.

(b) With maximum magnetic field strength of about 150 Gauss.

Fig.6 Ion current density profiles by Faraday cup with acceleration channel length of 20 mm at discharge voltage of 200 V and mass flow rate of 2 mg/s.

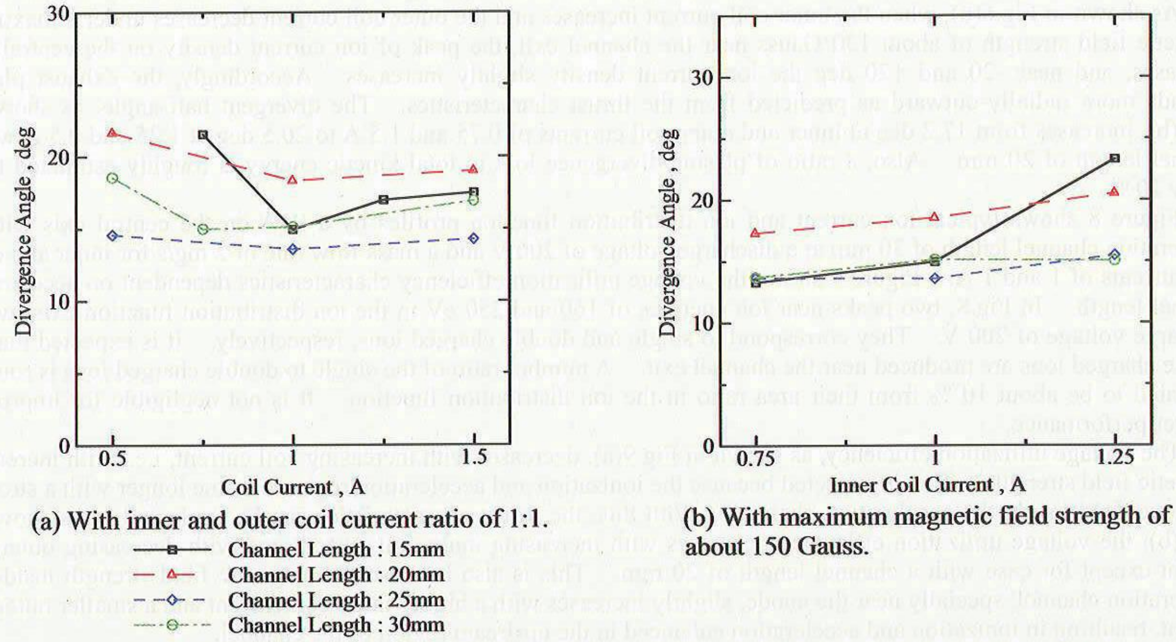

(a) With inner and outer coil current ratio of 1:1.

(b) With maximum magnetic field strength of about 150 Gauss.

Fig.7 Plasma plume divergent half-angle characteristics dependent on acceleration channel length at discharge voltage of 200 V and mass flow rate of 2 mg/s.

The performance characteristics was evaluated with an inner and outer coil current ratio of 1:1 dependent on acceleration channel length at a discharge voltage of 200 V and a mass flow rate of 2 mg/s. As shown in Fig.4, the maximum magnetic field strength near the channel exit was changed from 105 Gauss at 0.5 A to 210 Gauss at 1.5 A although the field shape was not changed. The discharge current characteristic had a minimum at a coil current of 1 A, i.e., at a maximum magnetic field strength of about 150 Gauss. The thrust and the specific impulse decreased with increasing magnetic field strength. The ratio of decrease was constant with channel lengths of 15 and 20 mm although it was very small with channel lengths of 25 and 30 mm. As a result, the thrust efficiency had a maximum near 150

Gauss. With a channel length of 20 mm, a high thrust efficiency of 40.1 % was achieved at a specific impulse of 1337 sec. These characteristics agreed with those for the THT-III thruster [7].

The performance characteristics was evaluated with a maximum magnetic field strength of about 150 Gauss dependent on acceleration channel length at a discharge voltage of 200 V and a mass flow rate of 2 mg/s. As shown in Fig.5, the magnetic field shape was changed with inner and outer coil currents of 0.75 and 1.5 A, 1 and 1 A; 1.25 and 0.5 A although the maximum field strength near the channel exit was kept about 150 Gauss. When the inner coil current increased and the outer coil current decreased, the thrust and the specific impulse decreased. This is expected because the magnetic field strength near the anode slightly becomes large, as shown in Fig.5(c), resulting in ionization and wall loss enhanced in the upstream region of the channel. As an another reason, it is considered that the exhaust plasma intensively expands radially-outward as predicted from the magnetic field lines in Figs.4 and 5; that is, the divergent angle of plasma plume becomes large as shown below. The discharge current also slightly decreased with increasing inner coil current although the ratio of decrease was very small. Accordingly, a maximum thrust efficiency was achieved with the smallest inner coil current of 0.75 A and the highest outer coil current of 1.5 A, and then it reached 41.2 % at a specific impulse of 1367 sec.

Accordingly, the thruster performance is very sensitive to acceleration channel length. The discharge current was the smallest with a channel length of 20 mm at a constant coil current although the thrust and specific impulse were the highest. As a result, the thrust efficiency was the highest with 20 mm. This is explained as follows. A short channel of 15 mm does not have an enough length for ionization. On the other hand, with long channels of 25 and 30 mm, ion losses on the channel wall are relatively large. Consequently, there exists an optimum channel length to achieve high performance.

2.2.2 Exhaust plasma plume characteristics

Figure 6 shows the ion current density profiles by a Faraday cup with an acceleration channel length of 20 mm at a discharge voltage of 200 V and a mass flow rate of 2 mg/s. Figure 7 shows the plasma plume divergent half-angle characteristics dependent on acceleration channel length. The divergent half-angle is calculated from a half-width of the fitting profile. As shown in Fig.6(a), the peak of ion current density on the central axis increases with coil current, i.e., with magnetic field strength, and in ranges from -60 to -20 deg and from +20 to +60 deg the ion current density decreases. As a result, an increase in magnetic field strength produces a more convergent ion beam. The divergent half-angle, as shown in Fig.7(a), decreases from 21.7 deg at 0.5 A to 18.2 deg at 1.5 A with a channel length of 20 mm.

As shown in Fig.6(b), when the inner coil current increases and the outer coil current decreases under a maximum magnetic field strength of about 150 Gauss near the channel exit, the peak of ion current density on the central axis decreases, and near -20 and +20 deg the ion current density slightly increases. Accordingly, the exhaust plasma expands more radially-outward as predicted from the thrust characteristics. The divergent half-angle, as shown in Fig.7(b), increases from 17.2 deg at inner and outer coil currents of 0.75 and 1.5 A to 20.5 deg at 1.25 and 0.5 A with a channel length of 20 mm. Also, a ratio of plasma divergence loss to total kinetic energy is roughly estimated to be below 10 %.

Figure 8 shows typical ion current and ion distribution function profiles by a RPA on the central axis with an acceleration channel length of 30 mm at a discharge voltage of 200 V and a mass flow rate of 2 mg/s for inner and outer coil currents of 1 and 1 A. Figure 9 shows the voltage utilization efficiency characteristics dependent on acceleration channel length. In Fig.8, two peaks near ion energies of 160 and 250 eV in the ion distribution function exist with a discharge voltage of 200 V. They correspond to single and double charged ions, respectively. It is expected that the double charged ions are produced near the channel exit. A number ratio of the single to double charged ions is roughly estimated to be about 10 % from their area ratio in the ion distribution function. It is not negligible for improving thruster performance.

The voltage utilization efficiency, as shown in Fig.9(a), decreases with increasing coil current, i.e., with increasing magnetic field strength. This is expected because the ionization and acceleration region become longer with a stronger magnetic field inside the acceleration channel. With this, the thrust characteristics can be explained. As shown in Fig.9(b), the voltage utilization efficiency decreases with increasing inner coil current and with decreasing outer coil current except for case with a channel length of 20 mm. This is also because the magnetic field strength inside the acceleration channel, specially near the anode, slightly increases with a higher inner coil current and a smaller outer coil current, resulting in ionization and acceleration enhanced in the upstream region of the channel.

In Fig.9, the voltage utilization efficiency is the highest at an acceleration channel of 20 mm with a constant magnetic field strength although it is relatively low at 15 and 30 mm. This dependence on channel length agrees with the thruster performance.

Ion acceleration features dependent on magnetic field strength are summarized as follows. With a high magnetic field strength inside the acceleration channel, ionization and acceleration occur in a relatively upstream region in the channel. Therefore, although ion beam divergence is suppressed, ion losses on the channel wall are enhanced. With a weak magnetic field, ion production and acceleration concentrate near the channel exit. Although ion beams are slightly expanded radially-outward, wall losses are very small. In magnetic field shape, on the viewpoint of plasma plume feature it is suitable that downstream directions perpendicular to magnetic field lines near the channel exit are parallel to the central axis or slightly radially-inward. As for acceleration channel length, total wall losses are relatively large with a long channel although an ionization and acceleration region is too short in a short channel.

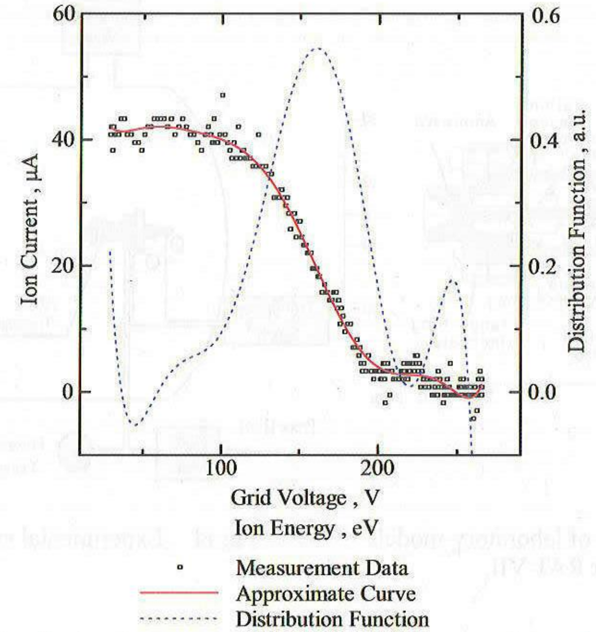

Fig.8 Ion current and ion distribution function profiles by retarding potential analyzer on central axis with 30 mm at 200 V and 2 mg/s for inner and outer coil currents of 1 and 1 A.

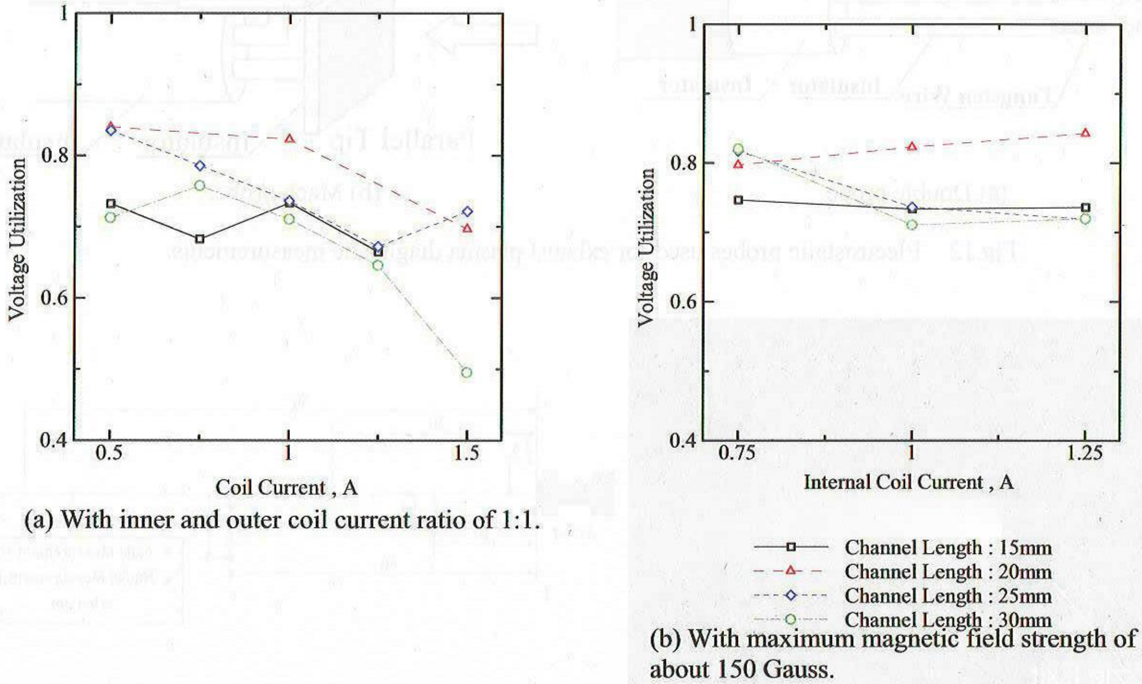

(a) With inner and outer coil current ratio of 1:1.

(b) With maximum magnetic field strength of about 150 Gauss.

Fig.9 Voltage utilization efficiency characteristics dependent on channel length for inner and outer coil currents of 1 and 1 A.at 200 V and 2 mg/s.

Consequently, an optimum magnetic field and channel structure is expected to exist under an operational condition, related to inner physical phenomena of plasma production, ion acceleration and exhaust plasma feature.

3. Direct-Current Arcjet Thruster

3.1 Experimental Apparatus

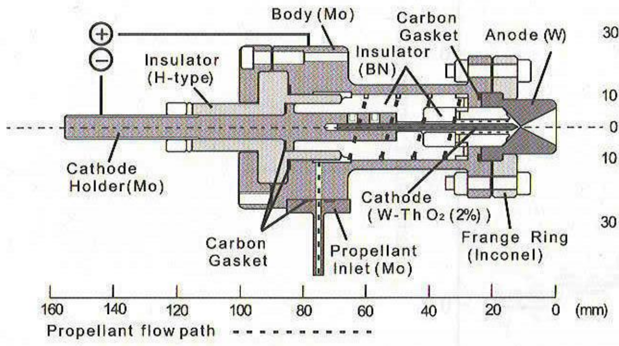

Fig.10 Cross-sectional view of laboratory-model radiation-cooled arcjet thruster RAT-VII.

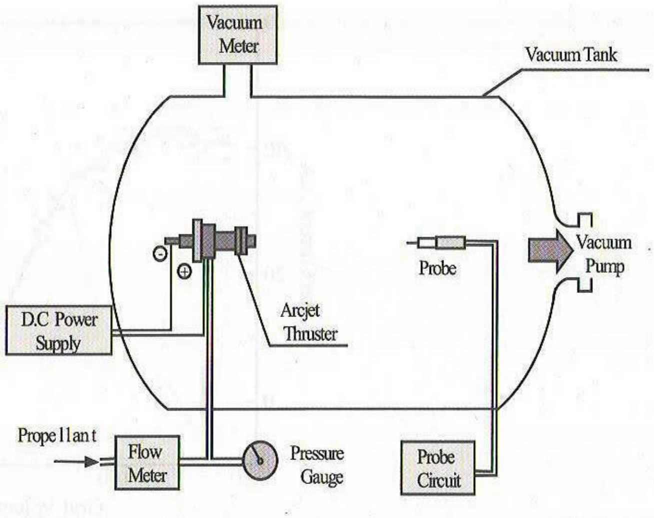

Fig.11 Experimental system of arcjet thruster.

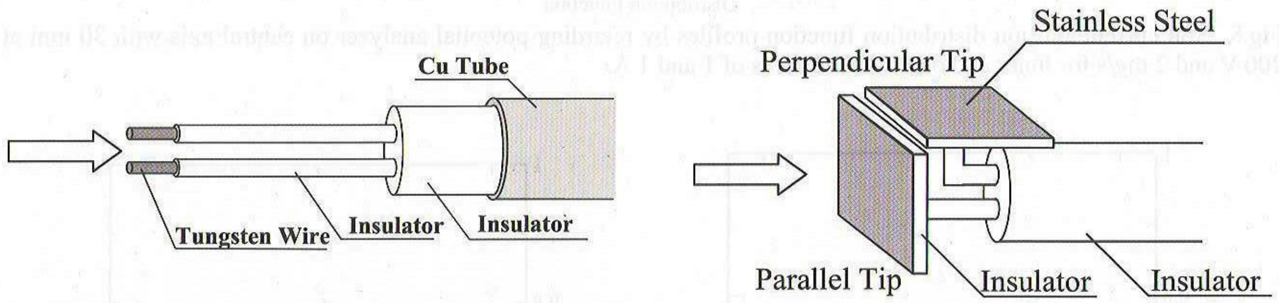

(a) Double probe.

(b) Mach probe.

Fig.12 Electrostatic probes used for exhaust plasma diagnostic measurements.

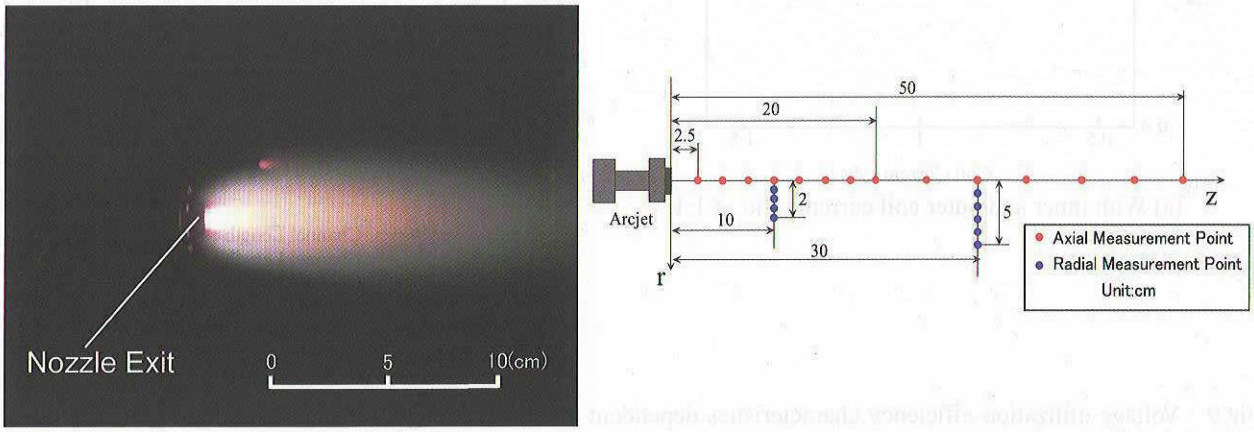

(a) Arcjet plasma plume feature.

(b) Measurement points

Fig.13 Arcjet plasma plume feature and all measurement points for electrostatic probes.

The cross-sectional view of the laboratory-model radiation-cooled arcjet thruster RAT-VII is shown in Fig.10. The cathode 2 mm in diameter, made of thoriated tungsten, has a conical angle 60 deg and a spherical tip 0.5 mm in radius. The tungsten anode with a constrictor 0.5 mm in diameter x 0.6 mm in length serves as an expansion nozzle with a conical convergent section 45 deg in half angle and a conical divergent section 30 deg in half angle. The

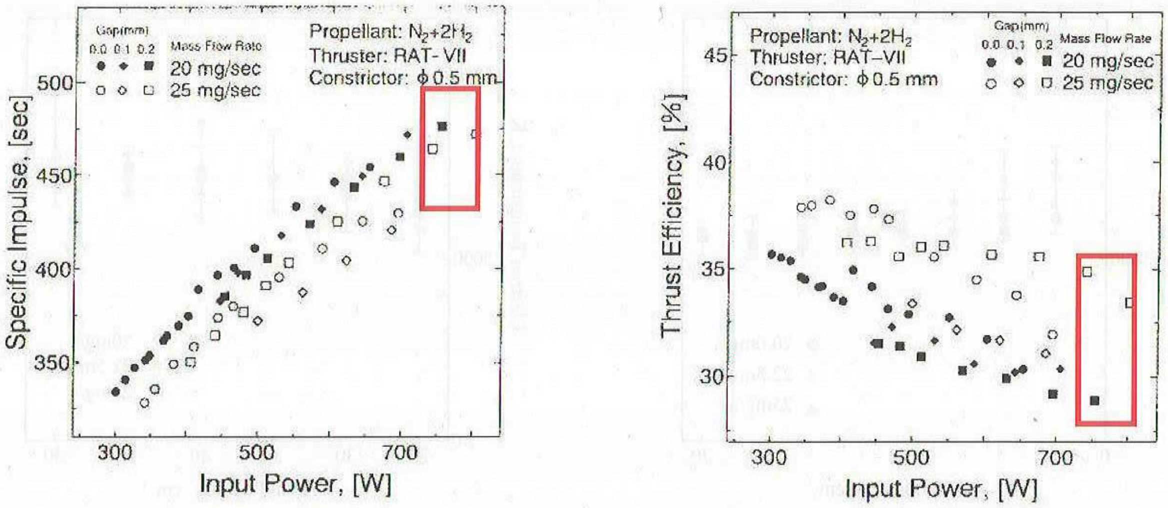

(a) Specific impulse.

(b) Thrust efficiency.

Fig.14 Specific impulse and thrust efficiency characteristics of laboratory-model radiation-cooled arcjet thruster RAT-VII dependent on input power.

expansion area ratio is 614. The electrode gap (the minimum axial distance between the cathode tip and the constrictor inlet) is set to 0.0-0.2 mm.

Propellant is introduced from a propellant inlet on the outer wall of the molybdenum body through a swirl passage on the inner wall and injected from the end of the cathode to the small arc chamber through the slits around the cathode rod. Thus, swirl flow is created for propellant gas injection. Vortex stabilization is expected to have some effects on steady-state arc stability and thruster performance [20]. Furthermore, the long propellant passage induces efficient regenerative cooling by the gas flow.

A mixture of hydrogen and nitrogen at a mixture ratio of 2:1 by volume is used as the propellant, simulating hydrazine decomposition products. The pure gases are stored in high-pressure bottles, then metered separately and mixed in the propellant feed line upstream of the thruster. The mixture enters the thruster at room temperature. Commercially-available thermal-conductivity-type mass flow controllers are used. The controllers were calibrated periodically using a volumetric method.

Power is supplied to the thruster from a 50 kHz pulse width modulated current regulated converter, which has potentials of high response and stable operation against current fluctuation. The power supply system is capable of delivering up to 150 V and 20 A to the thruster. Starting is facilitated by a built-in high-voltage circuit capable of providing a 2 kV pulse with 20 μ sec pulse width once every 160 msec until breakdown occurs.

All experiments are performed in a cylindrical vacuum tank 1.2 m in diameter and 2 m long, as shown in Fig.11. The ambient background pressure was between 5 and 20 Pa during operations. The thrust is determined by measuring with a load-cell a load due to a deflection of the water-cooled cantilevered hollow beam which supports the thruster [12-15]. The temperature at the location of the load cell is kept below 300 K during all experiments. Due to a ratio of the low thrust to the arcjet weight, thrust measurements were very sensitive to distortions of the vacuum tank due to thermal radiation to the tank wall and pressure difference. Drift was observed to be less than 3 % of the nominal thrust level. Therefore, the thrust measurement system is calibrated immediately at the operational thrust level after extinguishing the arc. Thrust calibration is conducted by a weight and pulley arrangement which is able to apply a known force to a thrust stand. With this design, friction force was small, and it resulted in no measurable hysteresis.

Exhaust plasma diagnostic measurements are carried out. Electrostatic probes are used for evaluation of electron temperature, electron number density and Mach number. A double probe, as shown in Fig.12(a), has a diameter of 0.4 mm and a length of 5 mm. The probe is located parallel to the central axis of the thruster near the arcjet exit, i.e., at axial positions from the arcjet exit to 20 cm downstream. The other double probe 6 mm in diameter x 50 mm in length is located at axial positions from 20 to 50 cm downstream. Radial profiles of plasma parameters are also measured at axial positions of 10 and 30 cm. In Mach number measurement, as shown in Fig.12(b), we use a special probe, called a Mach probe, with two plates 4 mm x 4 mm at an axial position of 10 cm and 30 mm x 10 mm at 30 cm. Mach number is evaluated from a ratio of the currents collected with the two plates parallel and perpendicular to plasma flow [21]. Figure 13 shows a plasma plume feature and all measurement points.

Operational parameters are monitored during all measurements, including discharge voltage and current, hydrogen and nitrogen mass flow rates and ambient background pressure. During nominal arcjet testing, an electrically isolated digital voltmeter is used to measure discharge voltage with a resolution of 0.1 V. Arc current is measured using a

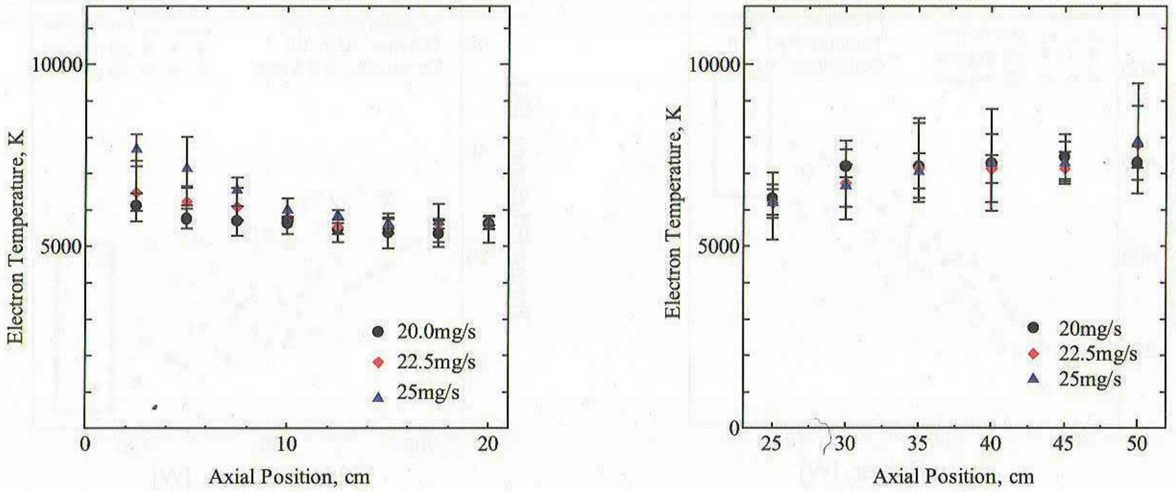

(a) From nozzle exit to 20 cm. (b) From 25 to 50 cm.

Fig.15 Axial distributions of electron temperature on central axis in the downstream region.

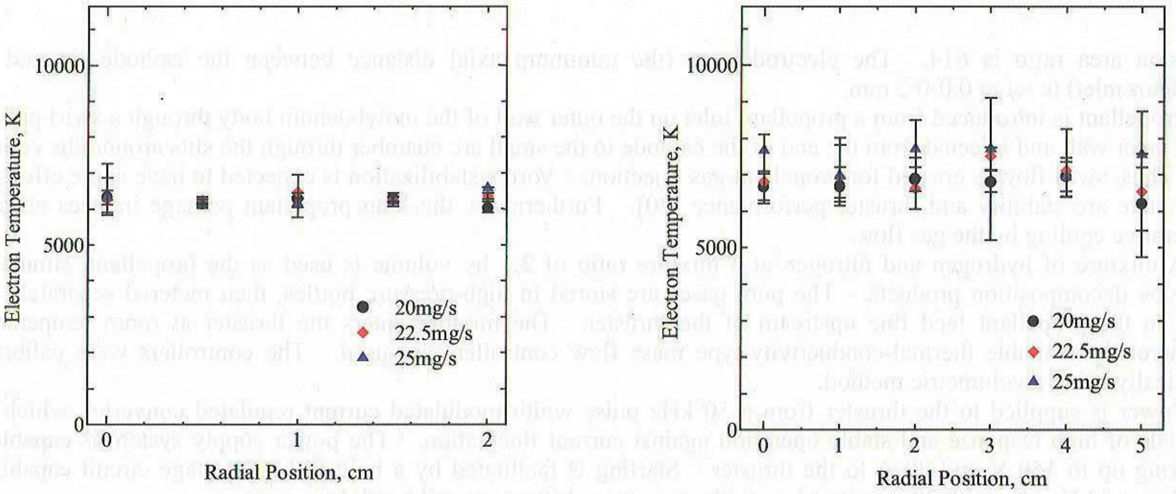

(a) At 10 cm. (b) At 30 cm.

Fig.16 Radial distributions of electron temperature at axial positions of 10 and 30 cm in the downstream region.

shunt in series with the thruster, which provides a resolution of 0.1 A.

3.2 Results and Discussion

3.2.1 Thruster performance

Figure 14 shows the specific impulse and thrust efficiency characteristics dependent on input power. The specific impulse increases from 330 sec at 300 W to 470 sec at 750 W with mass flow rates of 20 and 25 mg/s. On the other hand, the thrust efficiency decreases from 35-38 % at 300 W to 30-33 % at 750 W. Probe measurements are conducted in the rectangular region shown in Fig.14, in which specific impulses of 450-470 sec and thrust efficiencies of 30-35 % are achieved with mass flow rates of 20-25 mg/s at input powers of 750-800 W.

3.2.2 Exhaust plasma plume characteristics

Figure 15 shows the axial distributions of electron temperature on the central axis in the downstream region. The electron temperatures are 6000-8000 K, and their changes are small regardless of mass flow rate. The radial profiles, as shown in Fig.16, are also flat at axial positions of 10 and 30 cm. This is considered because energy exchange among light particles of electrons intensively occurs even in the low-pressure environment.

Figure 17 shows the axial distributions of electron number density on the central axis in the downstream region. The electron number density rapidly decreases from the order of 10^{18} m^{-3} near the nozzle exit to the order of 10^{14} m^{-3} at

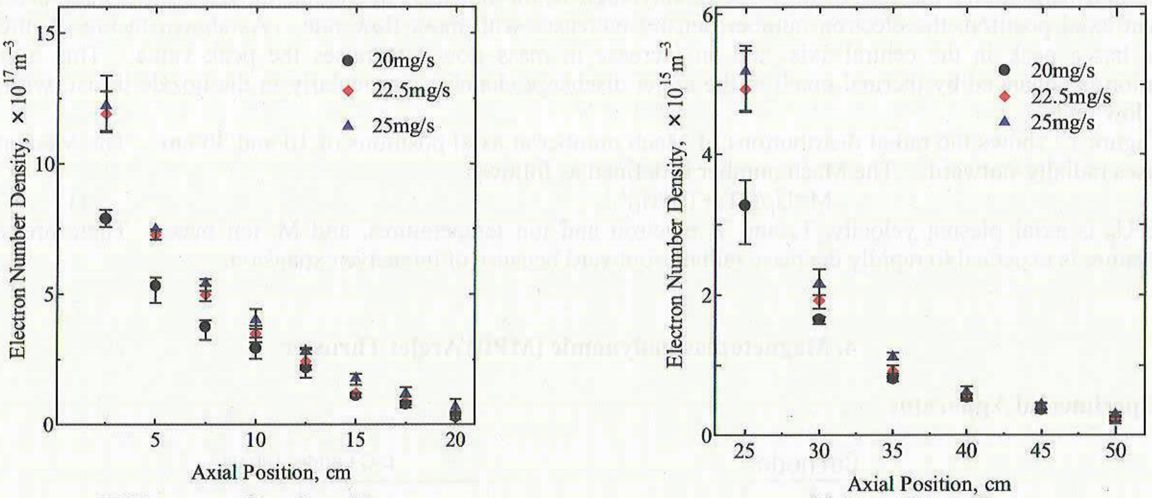

(a) From nozzle exit to 20 cm. (b) From 25 to 50 cm.

Fig.17 Axial distributions of electron number density on central axis in the downstream region.

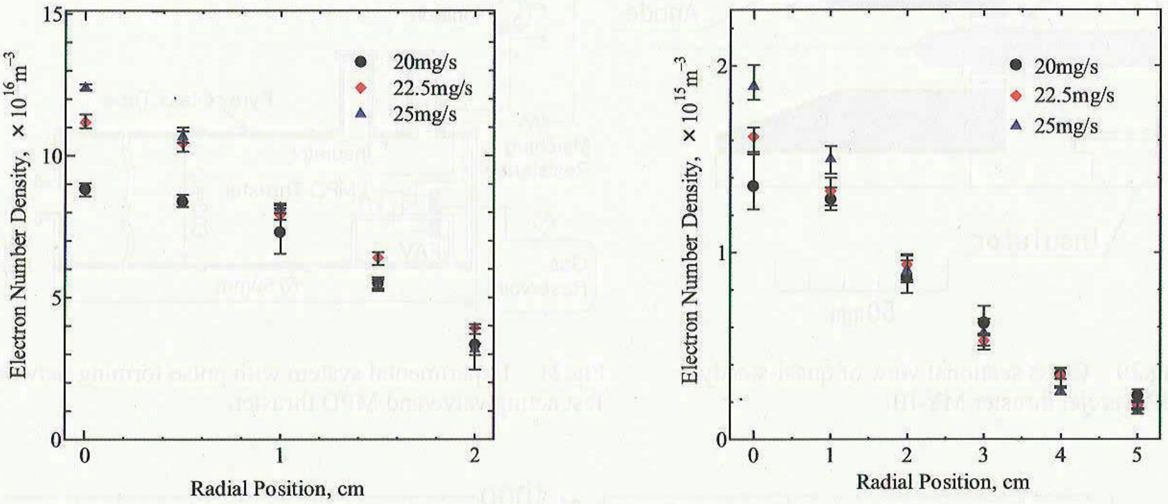

(a) At 10 cm. (b) At 30 cm.

Fig.18 Radial distributions of electron number density at axial positions of 10 and 30 cm in the downstream region.

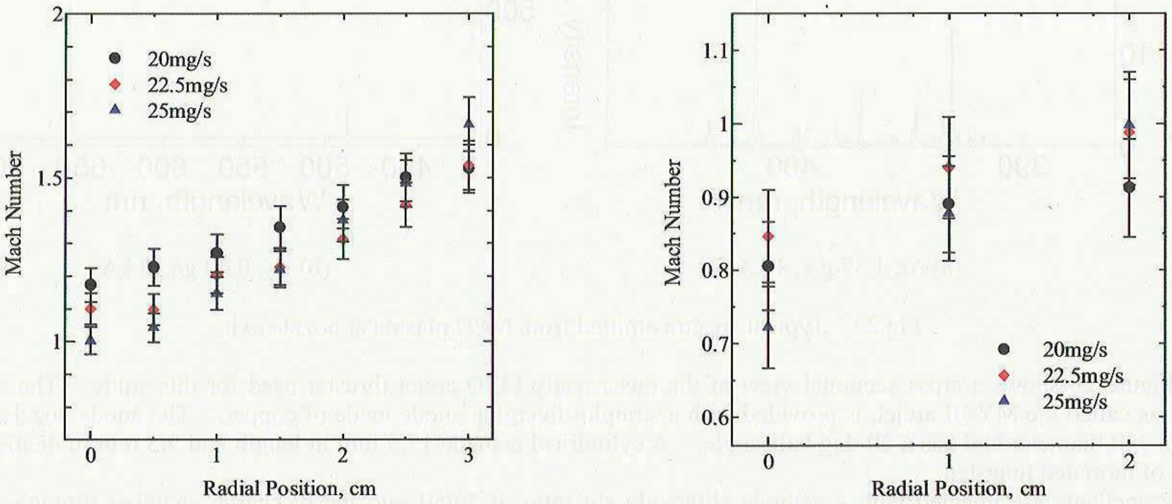

(a) At 10 cm. (b) At 30 cm.

Fig.19 Radial distributions of Mach number at axial positions of 10 and 30 cm in the downstream region.

50 cm, and particularly the rate of decrease is very high in the downstream region far from the nozzle exit. At a constant axial position, the electron number density increases with mass flow rate. As shown in Fig.18, the radial profile has a peak in the central axis, and an increase in mass flow rate raises the peak value. This is because ionization is enhanced by thermal pinch in the arcjet discharge chamber, particularly in the nozzle throat, with higher mass flow rates.

Figure 19 shows the radial distributions of Mach number at axial positions of 10 and 30 cm. The Mach number increases radially-outward. The Mach number is defined as follows:

$$M=U_p/((T_e+T_i)/M_i)^{1/2} \tag{1}$$

where U_p is axial plasma velocity, T_e and T_i electron and ion temperatures, and M_i ion mass. Therefore, the ion temperature is expected to rapidly decrease radially-outward because of intensive expansion.

4. Magnetoplasmadynamic (MPD) Arcjet Thruster

4.1 Experimental Apparatus

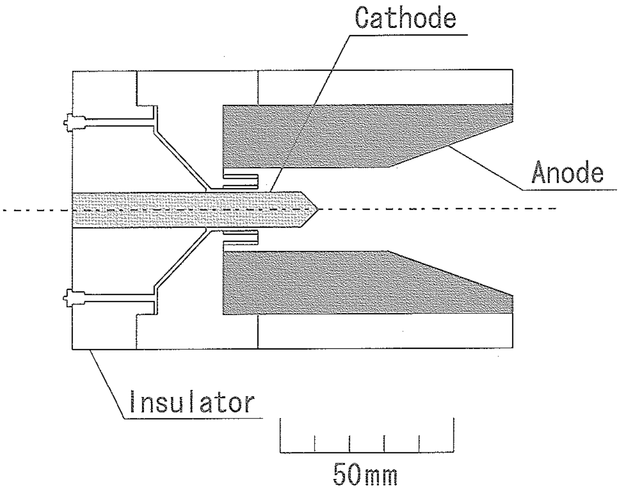

Fig.20 Cross sectional view of quasi-steady MPD arcjet thruster MY-III.

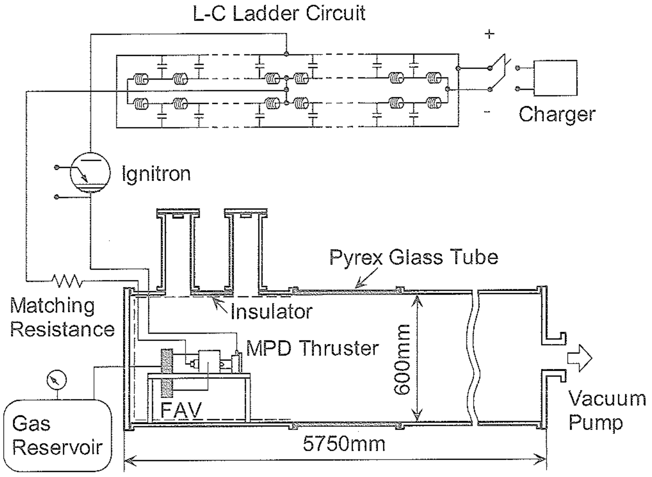

Fig.21 Experimental system with pulse forming network, fast acting valve and MPD thruster.

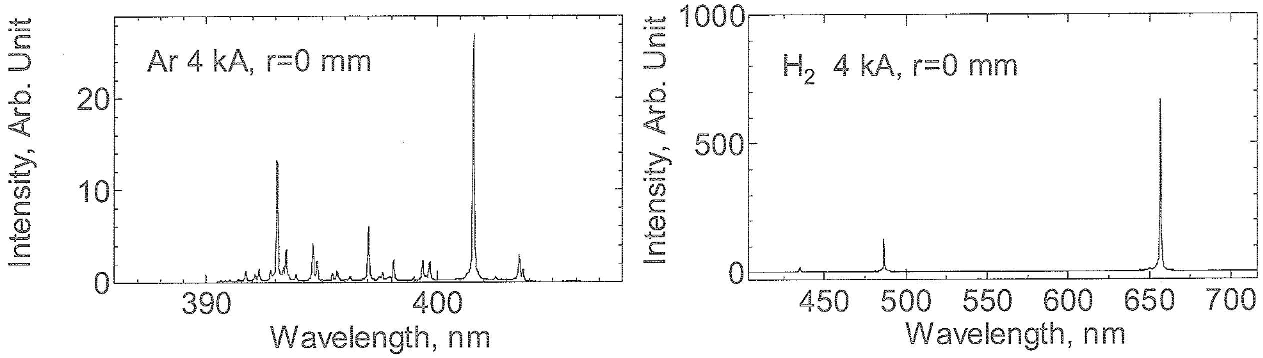

(a) Ar, 1.37 g/s, 4 kA.

(b) H_2, 0.40 g/s, 8 kA.

Fig.22 Typical spectra emitted from MPD plasma at nozzle exit.

Figure 20 shows a cross sectional view of the quasisteady MPD arcjet thruster used for this study. The arcjet, which is called the MY-III arcjet, is provided with a straight-diverging anode made of copper. The anode nozzle is 58 mm in exit diameter and has a 20-deg half-angle. A cylindrical cathode 17.5 mm in length and 9.5 mm in diameter is made of thoriated tungsten.

Propellants are injected with a cathode slit/anode slit ratio of 50/50 into the discharge chamber through a fast acting valve (FAV) fed from a high pressure reservoir. The rise time and width of the gas pulse, measured with a fast

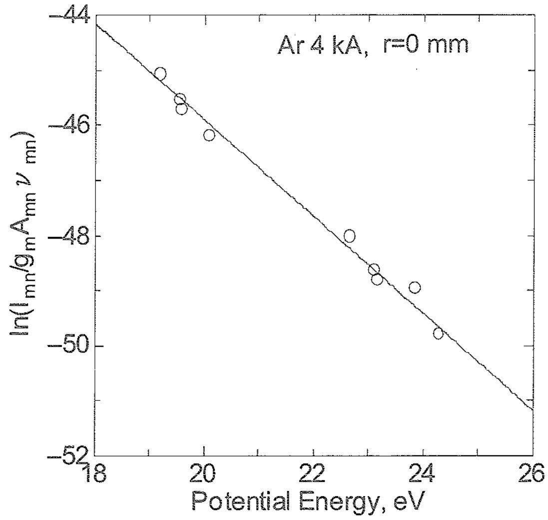

Fig.23 Typical Boltzmann plotting for determination of electronic excitation temperature with ArII lines at Ar, 1.37 g/s and 4 kA.

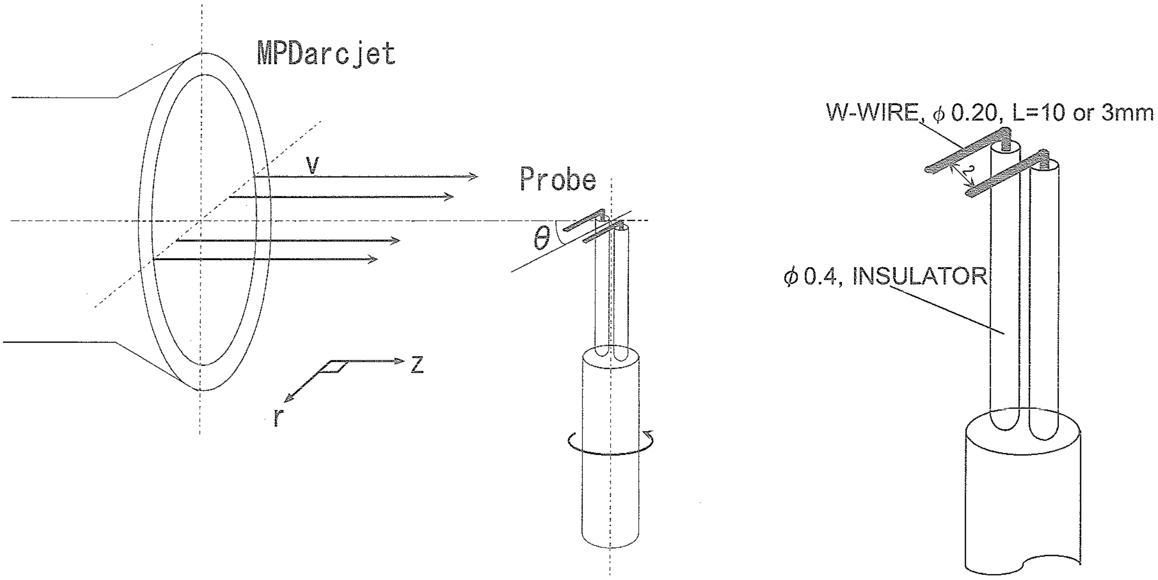

(a) probe and plasma flow arrangement.

(b) probe structure.

Fig.24 Rotatable electrostatic double probe system for measurement of plasma flow direction, electron temperature and plasma number density.

ionization gauge, are 0.5 and 6 msec, respectively. Hydrogen and argon are used as the propellant. The mass flow rates are controlled by adjustment of the reservoir pressure and the orifice diameter of the FAV.

As shown in Fig.21, the main power-supplying pulse forming network, which is capable of storing 62 kJ at 8 kV, delivers a single nonreversing quasisteady current of a maximum of 27 kA with a pulse width of 0.6 msec. A vacuum tank 5.75 m in length and 0.6 m in diameter, where the arcjet is fired, is evacuated to some 10^{-3} Pa prior to each discharge.

Discharge currents are measured by a Rogowski coil calibrated with a known shunt resistance. Voltage measurement is performed with a current probe (Iwatsu CP-502), which detects the small current bled through a known resistor (10 kΩ) between the electrodes.

Emission spectroscopic measurement is conducted as reliable plasma disgnostic ones both inside and outside the discharge chamber. Light comes from MPD plasma. Then, the emission is collected by a lens of 80 mm in focal length and is introduced into a 0.5 m monochrometer through an optical fiber. The monochrometer of diffraction-grating-type HAMAMATSU C5095 is provided with a 2400 grooves/mm grating plate and a 1024-channel

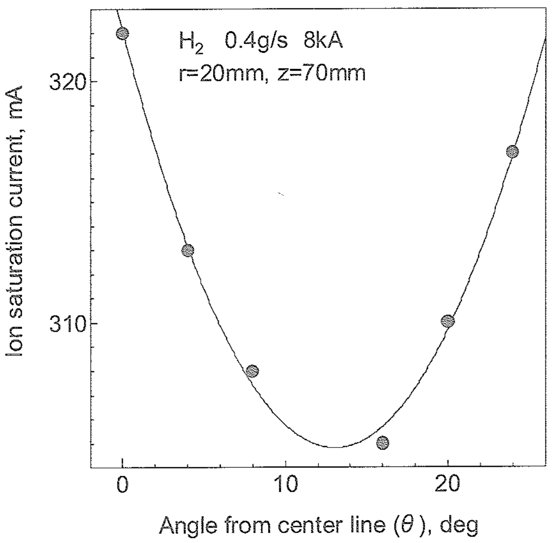

Fig.25 Typical characteristics of ion saturation current of rotatable double probe dependent on angle of probe line to plasma flow.

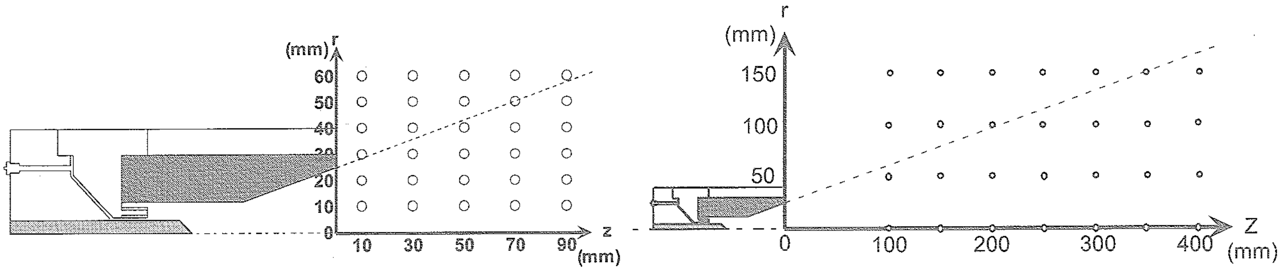

(a) near divergent nozzle exit.

(b) downstream region.

Fig.26 Measurement points for rotatable double probe.

diode array detector, achieving a spectral resolution of 0.05 nm per detector channel. The measurement is conducted in a steady-state condition by avoiding transitional phenomena near the start of the discharge. The emission is measured for a period of 0.4 msec after 0.2 msec from the discharge ignition. The timing is controlled with a gate of the image intensifier, which can open or close the entrance to the array detector.

Electron number densities and electronic excitation temperatures are determined using the spectral data. Because the electronic excitation temperature is almost equal to the free electron temperature in MPD plasma conditions, the former is called electron temperature in this paper. The electron number density is estimated from the stark width of the hydrogen H_β line 486.1 nm. For Ar gas, a small amount of H_2 is added. The spectral intensities measured in this experiment are line-of-sight values, measured by looking through the arc from the side perpendicular to the central line of the arcjet. For line-of-sight measurements, the intensity values correspond to the integrated values of intensity as a function of position. The radially dependent emission coefficient is determined from the measured intensities using well-known Abel transformations. The horizontally average spectral intensities are measured with a vertical interval of 1.0 mm. As shown in Figs.22 and 23, the Ar^+-ion electronic excitation temperature is determined with several ArII lines using a relative intensity method of spectral lines, i.e., by means of Boltzmann plotting, under the assumption of local thermodynamical equilibrium. The H-atom electronic excitation temperature is also determined with HI Balmer lines of 434.0, 486.1 and 656.3 nm.

Electrostatic double probe measurement is carried out to examine exhaust plasma plume features. Electron temperatures and ion (electron) number densities are evaluated. Furthermore, as shown in Fig.24, plasma flow directions are inferred with a rotatable cylindrical probe. When rotating the probe, the ion saturation current, as shown in Fig.25, has a minimum at the special condition that the plasma flows parallel to the probe axis. We can determine a flow direction from the angle. As shown in Fig.26, measurements are conducted in a large region downstream from the arcjet nozzle exit.

4.2 Results and Discussion

4.2.1 Plasma characteristics at nozzle exit

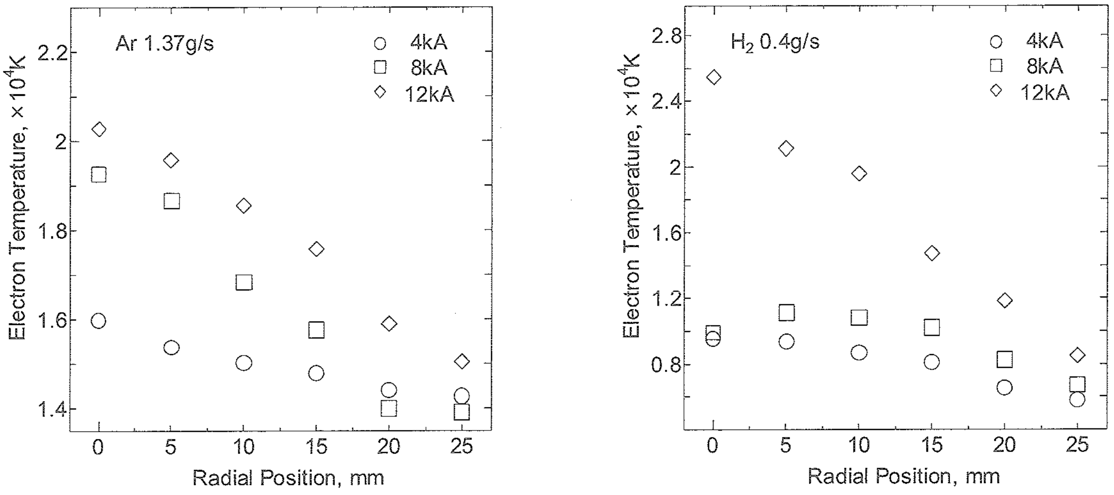

(a) Ar, 1.37 g/s. (b) H_2, 0.40 g/s.

Fig.27 Radial distributions of electron temperature on arcjet nozzle exit with Ar and H_2 by emission spectroscopic measurement.

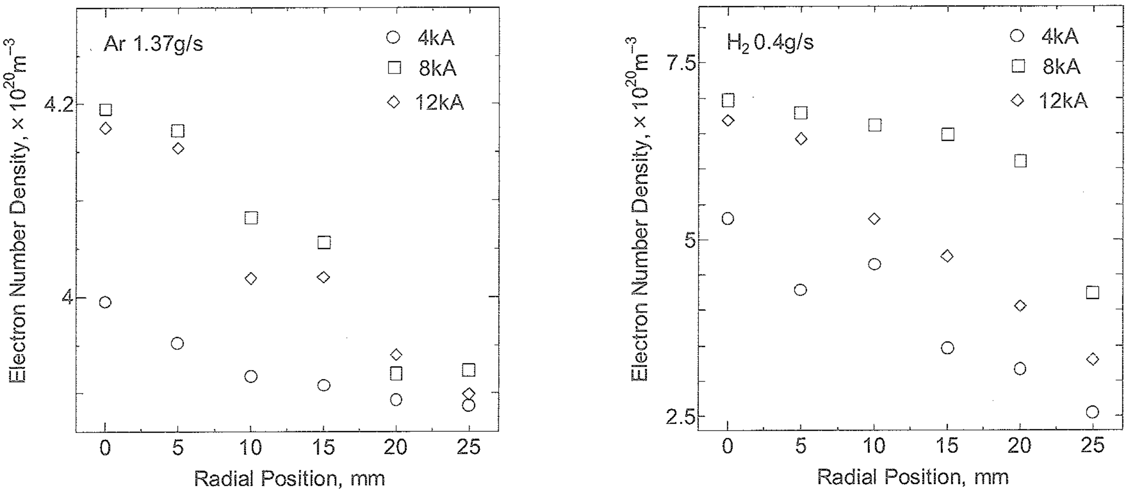

(a) Ar, 1.37 g/s. (b) H_2, 0.40 g/s.

Fig.28 Radial distributions of plasma number density on arcjet nozzle exit with Ar and H_2 by emission spectroscopic measurement.

Figures 27 and 28 show the radial distributions of electron temperature and plasma number density, respectively, on the arcjet nozzle exit with Ar and H_2. They are estimated from spectroscopic measurement. Both the electron temperature and the plasma number density have peaks at the central axis and decrease radially outward with a constant discharge current regardless of gas species.

As shown in Fig.27, the electron temperature increases with discharge current at a constant radial position, and particularly at the highest discharge current of 12 kA the electron temperature reaches above 20000 K at the center. However, it decreases to about 15000 K for Ar and about 8000 K for H_2 at a radial position of 25 mm regardless of discharge current; that is, the electron temperature intensively decreases radially outward at 12 kA although it gradually decreases at 4 kA for Ar and at 4 and 8 kA for H_2.

In the plasma number density characteristics, as shown in Fig.28, the Ar plasma densities at 8 and 12 kA are higher than that at 4 kA at a constant radial position although they decrease to about 3.9×10^{20} m^{-3} at 25 mm regardless of discharge current. The profile at 8 kA is almost the same one at 12 kA. In other words, the plasma density intensively decreases radially outward at 8 and 12 kA although it gradually decreases at 4 kA. For H_2, the plasma

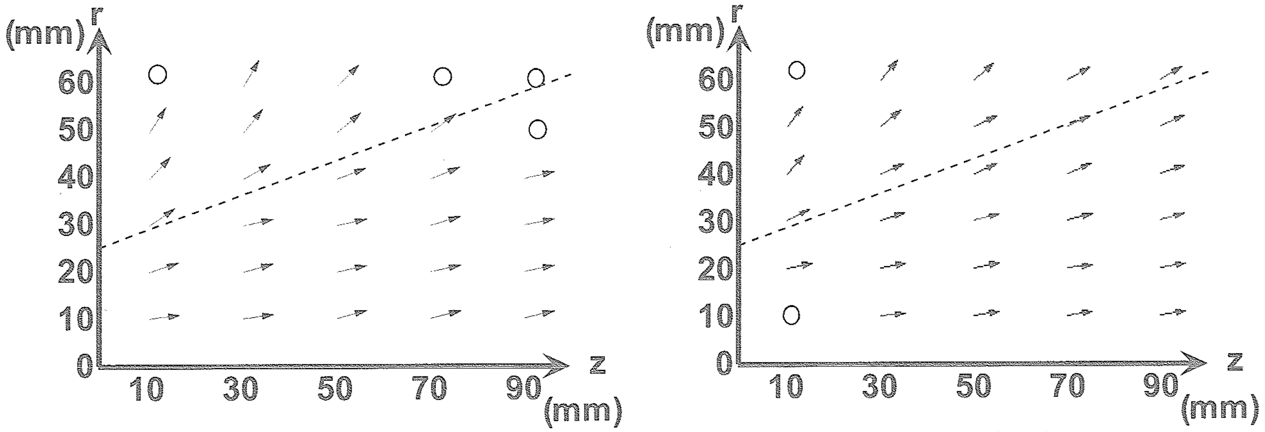

(a) Ar, 1.37 g/s, 4 kA. (b) Ar, 1.37 g/s, 8 kA.

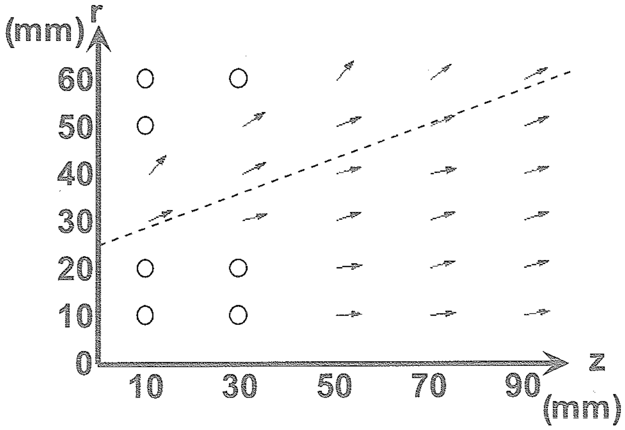

(c) H_2, 0.40 g/s, 8 kA.

Fig.29 Plasma flow patterns in exhaust plumes from nozzle exit to axial position of 90 mm with Ar and H_2. The dashed lines represent the extrapolation line of the divergent nozzle.

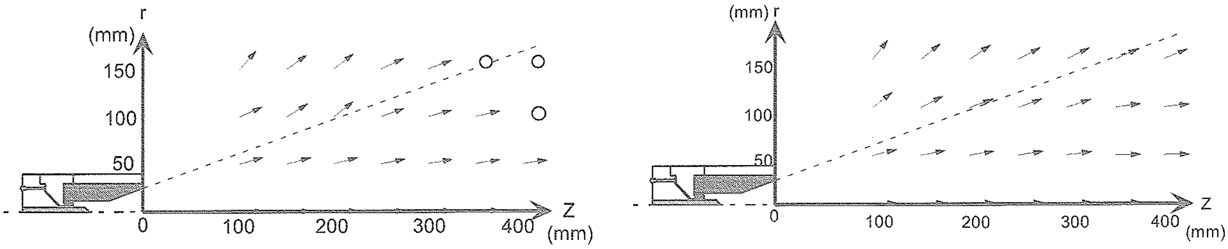

(a) Ar, 1.37 g/s, 4 kA. (b) Ar, 1.37 g/s, 8 kA.

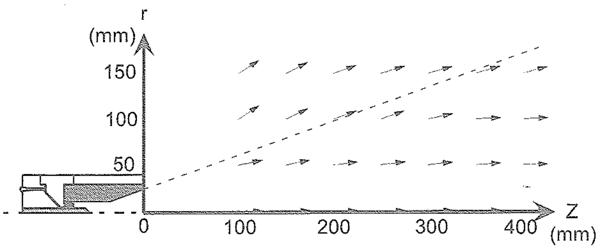

(c) H_2, 0.40 g/s, 8 kA.

Fig.30 Plasma flow patterns in exhaust plumes from axial position of 100 mm to 400 mm with Ar and H_2. The dashed lines represent the extrapolation line of the divergent nozzle.

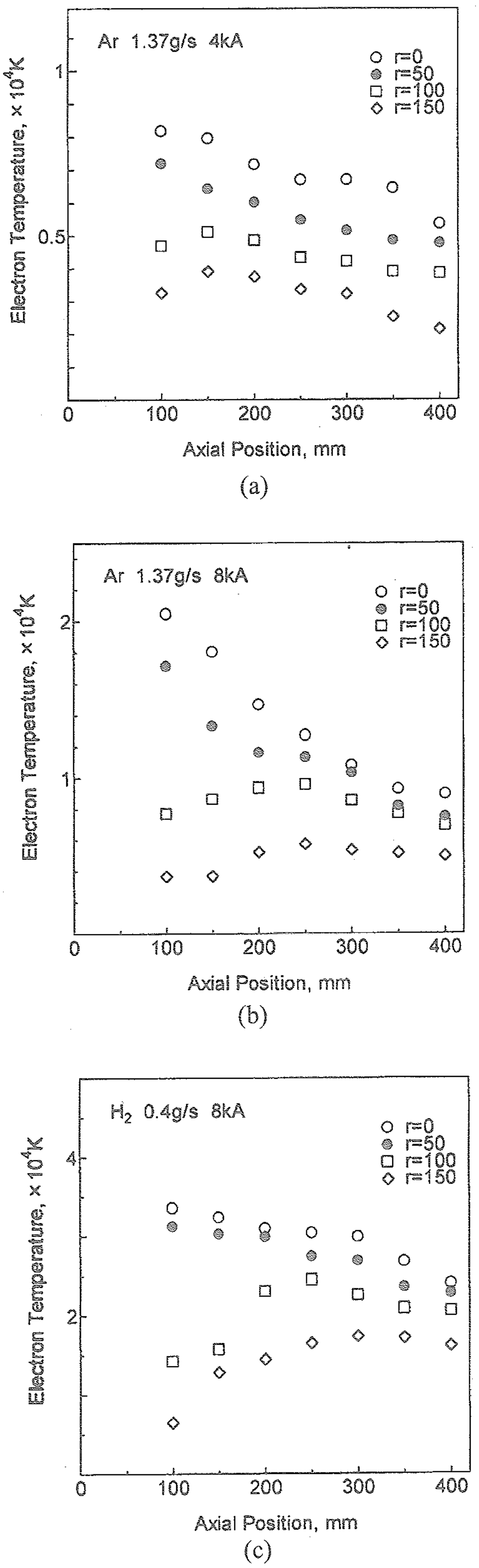

(a)

(b)

(c)

Fig.31 Axial distributions of electron temperature in exhaust plumes with Ar and H_2 by double probe measurement. (a) Ar, 1.37 g/s, 4 kA; (b) Ar, 1.37 g/s, 8 kA; (c) H_2, 0.40 g/s, 8 kA.

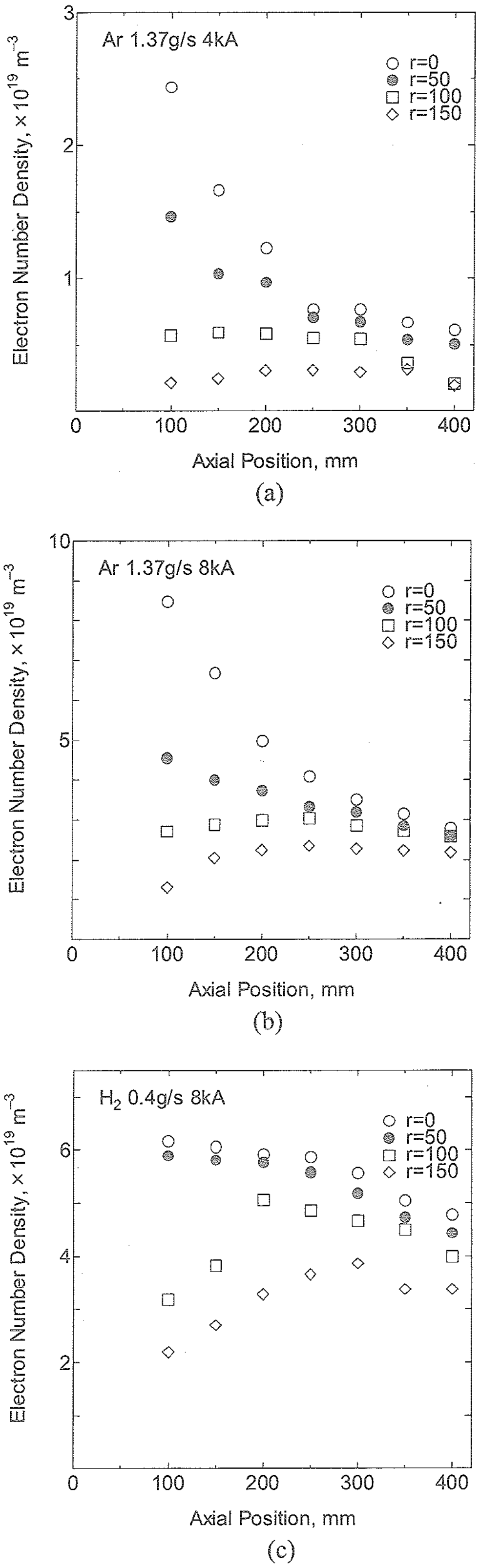

(a)

(b)

(c)

Fig.32 Axial distributions of plasma number density in exhaust plumes with Ar and H_2 by double probe measurement. (a) Ar, 1.37 g/s, 4 kA; (b) Ar, 1.37 g/s, 8 kA; (c) H_2, 0.40 g/s, 8 kA.

density at 8 kA is higher than that at 12 kA at a constant radial position, and at 4 kA it is the lowest. The profile at 8 kA is a flat-like one near the central axis. This is expected because the plasma at 12 kA is intensively pinched, thermally and electromagnetically, radially inward near the central axis, i.e., in the cathode jet, compared with the case at 8 kA. In other words, a radially broad plasma is created at 8 kA.

4.2.2 Plasma parameters and plasma flow direction in exhaust plume

Figures 29 and 30 show the plasma flow patterns in the exhaust plumes from the nozzle exit to an axial position of 90 mm and from 100 to 400 mm, respectively. Only the direction of arrows is important, and the length is arbitrary ones. The dashed lines represent the extrapolation line of the divergent nozzle. The plasma is slightly expanded radially outward downstream within the dashed line, i.e., the nozzle extrapolation line, regardless of gas species; then, near the central axis, i.e., in the cathode jet, it almost flows parallel to the axis, although it is intensively expanded outside the line. In other words, the angle of radial expansion is below the half angle of the nozzle, 20 deg, within the dashed line although it is above the half angle outside the dashed line. Therefore, the plasma flow is divided into inner and outer flows with the nozzle extrapolation line.

As shown in Figs.29(a), 29(b), 30(a) and 30(b), the radial expansion of the Ar plasma at 4 kA is relatively large compared with that at 8 kA. This is expected because the plasma is with a higher axial velocity at a larger discharge current. When comparing the pattern at 8 kA for H_2 with that for Ar, as shown in Figs.29(b), 29(c), 30(b) and 30(c), the angle of radial expansion for H_2 is relatively small because of an intensive thermal pinch effect for H_2.

Figures 31 and 32 show the axial distributions of electron temperature and plasma number density, respectively, in the exhaust plumes. They are estimated from probe measurement. Both the electron temperature and the plasma number density decrease radially outward at a constant axial position. They decrease downstream at radial positions of 0 and 50 mm, i.e., within a radial position of 50 mm, although they have peaks at 100 and 150 mm regardless of gas species. The peaks are located near the boundary between the inner and outer flows, i.e., near the extrapolation line of the divergent nozzle. Therefore, it is inferred that an intensive radial expansion occurs in the outer flow and that the electron temperature and the plasma density are seen to decrease axially. In the inner flow, a large amount of thermal energy is expected to be smoothly converted downstream into axial kinetic energy, and the axial plasma acceleration decreases both the physical properties.

As shown in Figs.31(a) and 31(b), the electron temperature for Ar at 4 kA gradually decreases downstream with radial positions of 0 and 50 mm. However, the temperature at 8 kA extremely decreases although, at enough downstream positions of 300-400 mm, it hardly changes and about 7000 K. Also, the Ar plasma densities at 4 and 8 kA, as shown in Figs.32(a) and 32(b), intensively decrease axially within a radial position of 50 mm although they are almost kept 5×10^{18} m^{-3} at 4 kA and 2.5×10^{19} m^{-3} at 8 kA at axial positions of 300-400 mm. For H_2, both the distributions of electron temperature and plasma density, as shown in Figs.31(c) and 32(c), are almost flat from an axial position of 100 mm to about 300 mm within a radial position of 50 mm, and they gradually decrease to about 22500 K to about 4.5×10^{19} m^{-3}, respectively, downstream from 300 mm. At radial positions of 100 and 150 mm, both the properties intensively increase axially from 100 to 200-250 mm and then gradually decrease downstream. Therefore, a distinct boundary between the inner and outer flows is created with H_2. As shown in Figs.31(b), 31(c), 32(b) and 32(c), the electron temperature for H_2 is relatively large compared with that for Ar, and the plasma density for H_2 is also larger at enough downstream positions of 300-400 mm than that for Ar. This is expected because of the intensive pinch effect for H_2.

5. Conclusions

The laboratory-model low-power Hall-effect thruster THT-IV could be stably operated with a highest performance under an optimum acceleration channel length of 20 mm and an optimum magnetic field with a maximum strength of about 150 Gauss near the channel exit and with some shape considering ion acceleration directions. With a higher magnetic field strength inside the acceleration channel, ionization and acceleration occur in a relatively upstream region in the channel. Therefore, although ion beam divergence is suppressed, ion losses on the channel wall are enhanced. With a weaker magnetic field, ion production and acceleration concentrate near the channel exit. Although ion beams are slightly expanded radially-outward, wall losses are very small. In magnetic field shape, it is suitable that downstream directions perpendicular to magnetic field lines near the channel exit are parallel to the central axis or slightly radially-inward. As for acceleration channel length, total wall losses are relatively large with a longer channel although an ionization and acceleration region is too short in a shorter channel. Consequently, an optimum magnetic field and channel structure is considered to exist under an operational condition, related to inner physical phenomena of plasma production, ion acceleration and exhaust plasma feature.

The laboratory-model radiation-cooled arcjet thruster RAT-VII was operated in a low power range of 750-800 W with a mixture of hydrogen and nitrogen simulating hydrazine at mass flow rates of 20-25 mg/s in order to study the exhaust plasma plume characteristics. Electrostatic probe measurements were carried out to evaluate electron temperature, electron number density and Mach number in the downstream plume region. The electron temperature characteristics were almost flat ranging from 6000 to 8000 K. The electron number density on the central axis intensively decreased from the order of 10^{18} m^{-3} near the nozzle exit to the order of 10^{14} m^{-3} at an axial position of 50 cm. The electron density decreased radially-outward at a constant axial position although the Mach number increased. An increase in mass flow rate raised the electron number density, particularly on the central axis because of thermal pinch in the thruster discharge chamber.

The quasi-steady MPD thruster MY-III was operated to study the exhaust plume characteristics. Both emission spectroscopic and rotatable double probe measurements were made to evaluate electron temperatures, plasma number densities and plasma flow directions in the downstream plume region. The plasma was slightly expanded radially outward downstream within the extrapolation line of the divergent nozzle regardless of discharge current and gas species although it was intensively expanded outside the line. Therefore, the plasma flow was divided into inner and outer flows with the nozzle extrapolation line. Both the electron temperature and the plasma number density decreased radially outward at a constant axial position. In the outer flow, radial expansion intensively occurred, and both the properties were seen to decrease axially. In the inner flow, a large amount of thermal energy was expected to be smoothly converted downstream into axial kinetic energy, and the axial plasma acceleration decreased the electron temperature and the plasma density. The angle of radial expansion decreased with discharge current because of increasing axial velocity. The angle for H_2 was relatively small compared with cases for Ar because of an intensive thermal pinch effect for H_2.

References

[1] Kim, V.," Main Physical Features and Processes Determining the Performance of Stationary Plasma Thrusters," J. Propulsion and Power, Vol.14, 1998, pp.736-743.

[2] Dunning, J.W., Benson, S. and Oleson, S.," NASA's Electric Propulsion Program," 27th International Electric Propulsion Conference, Paper No.IEPC 01-002, 2001.

[3] Cadiou, A., Gelas, C., Darnon, F., Jolivet, L. and Pillet, N.," An Overview of the CNES Electric Propulsion Program," 27th International Electric Propulsion Conference, Paper No.IEPC 01-008, 2001.

[4] Tahara, H., Nikai, Y., Yasui, T. and Yoshikawa, T.," Hall Thruster Research at Osaka University," AIAA Paper No.99-2570, 1999.

[5] Goto, D., Tahara, H., Nikai, Y., Yasui, T. and Yoshikawa, T.," Research and Development of Hall Effect Thrusters at Osaka University," Proceedings of the 26th International Electric Propulsion Conference, Vol.1, Paper No.IEPC 99-121, 1999, pp.675-682.

[6] Tahara, H., Mitsuo, K., Goto, D., Yasui, T. and Yoshikawa, T.," Operating Characteristics of Low Power Hall Thrusters," 22nd International Symposium on Space Technology and Science, Paper No.ISTS 2000-b-36p, 2000.

[7] Tahara, H., Goto, D., Yasui, T. and Yoshikawa, T.," Thrust Performance and Plasma Characteristics of Low Power Hall Thrusters," 27th International Electric Propulsion Conference, Paper No.IEPC 01-042, 2001.

[8] Shirasaki, A., Tahara, H. and Martinez-Sanchez, M.," One-Dimensional Flowfield Calculation of Hall Thrusters," 23rd International Symposium on Space Technology and Science, Paper No.ISTS 2002-b-33p, 2002.

[9] Tahara, H., Fujioka, T., Shirasaki, A. and Yoshikawa, T.," Simple One-Dimensional Calculation of Hall Thruster Flowfields," 28th International Electric Propulsion Conference, Paper No.IEPC 03-016, 2003.

[10] Kitano, T., Fujioka, T., Shirasaki, A., Goto, D., Tahara, H., Yasui, T., Yoshikawa, T., Fuchigami, K., Iinoya, F. and Ueno, F.," Research and Development of Low Power Hall Thrusters," 23rd International Symposium on Space Technology and Science, Paper No.ISTS 2002-b-18, 2002.

[11] Kuninaka, H.," Activities on Electric Propulsion in Japan -Space Flight from Basic Research-," AIAA Paper No.2002-3563, 2002.

[12] Yoshikawa, T., Onoe, K., Yasuda, Y., Uematsu, K. and Ishii, M.," Endurance Tests of a Low Power Arcjet Thruster with Hydrogen/Nitrogen Propellant Mixture," AIAA Paper No. 90-2577, 1990.

[13] Yoshikawa, T., Onoe, K., Tsuri, S., Ishii, M. and Uematsu, K.," Development of a Low Power Arcjet Thruster -Thrust Performance and Life Evaluation-," Proceedings of the 22nd International Electric Propulsion Conference, Vol.1, Paper No.IEPC 91-043, 1991.

[14] Tsuri, S., Onoe, K., Yoshikawa, T., Ishii, M. and Uematsu, K.," Life Evaluation of a Low Power Arcjet Thruster," Proceedings of the 18th International Symposium on Space Technology and Science, Vol.1, 1992, pp.287-295.

[15] Yamamoto, Y., Onoe, K., Tahara, H., Yoshikawa, T., Ishii, M. and Sato, K.," Thrust Performance and Life Evaluation of a 1-kW-Class Arcjet Thruster," Proceedings of the 19th International Symposium on Space Technology and Science, Paper No.ISTS 94-a-53, 1994.

[16] Tahara, H., Uda, N., Onoe, K., Tsubakishita, Y. and Yoshikawa, T." Discharge Features in a Steady-State Nitrogen Arcjet Engine with an Expansion Nozzle," IEEE Trans. Plasma Science, Vol.22, 1994, pp.58-64.

[17] Tahara, H., Komiko, K., Yonezawa, T., Andoh, Y. and Yoshikawa, T." Thermodynamical Nonequilibrium Nitrogen Plasmas in a Direct-Current Arcjet Engine Nozzle," IEEE Trans. Plasma Science, Vol.24, 1996, pp.218-225.

[18] Tahara, H., Yonezawa, T., Andoh, Y. and Yoshikawa, T." Emission Spectroscopic Measurement of Ammonia or Mixture of Nitrogen and Hydrogen Plasma in a Direct-Current Arc Jet Generator with an Expansion Nozzle," IEEE Trans. Plasma Science, Vol.26, 1998, pp.1307-1313.

[19] Tahara, H., Ando, Y. and Yoshikawa, T." Plasma and Heat Flux Characteristics of a Supersonic Ammonia or

Nitrogen/Hydrogen-Mixture Direct-Current Plasma Jet Impinging on a Flat Plate," IEEE Trans. Plasma Science, Vol.31, 2003, pp.281-288.

[20] Tahara, H., Taniguchi, T., Onoe, K. and Yoshikawa, T.," DC Arcjet Plasma Characteristics Using Ammonia and Mixture of Nitrogen and Hydrogen," AIAA Paper No. 99-3736, 1999.

[21] Ando, A. and Hattori, K.," Mach-Probe Characteristics in a Magnetized Flow," Proceedings of the 26th International Electric Propulsion Conference, Paper No.IEPC 99-180, 1999, pp.1040-10145.

[22] Uematsu, K. and Kuriki, K.," Effect of Electrode Configuration on MPD Arcjet Performance," 17th International Electric Propulsion Conference, Paper No.IEPC 84-11, 1984.

[23] Tahara, H., Kagaya, Y. and Yoshikawa, T.," Effects of Applied Magnetic Fields on Performance of Quasisteady Magnetoplasmadynamic Arcjet," J. Propulsion and Power, Vol.11, 1995, pp.337-342.

[24] Mitsuo, K., Tahara, H., Okutani, H., Kagaya, Y. and Yoshikawa, T.," Experimental and Analytical Study of Quasi-Steady MPD Channel Flow," 25th International Electric Propulsion Conference, Paper No.IEPC 97-111, 1997.

[25] Tahara, H., Yamasaki, N., Mitsuo, K., Kagaya, Y. and Yoshikawa, T.," Plasma Features near Quasisteady Magnetoplasmadynamic Arcjet Cathodes," 25th International Electric Propulsion Conference, Paper IEPC 97-118, 1997.